Multiphase imaging of gas flow in a nanoporous material using remote-detection NMR

ELAD HAREL, JOSEF GRANWEHR*, JULIETTE A. SEELEY[†] AND ALEX PINES[‡]

Materials Sciences Division, Lawrence Berkeley National Laboratory, and Department of Chemistry, University of California, Berkeley, California 94720, USA
*Present address: Sir Peter Mansfield Magnetic Resonance Centre, University of Nottingham, Nottingham NG7 2RD, UK
[†]Present address: MIT Lincoln Laboratory, 244 Wood St., Lexington, Massachusetts 02420, USA
[‡]e-mail: pines@cchem.berkeley.edu

Pore structure and connectivity determine how microstructured materials perform in applications such as catalysis, fluid storage and transport, filtering or as reactors. We report a model study on silica aerogel using a time-of-flight magnetic resonance imaging technique to characterize the flow field and explain the effects of heterogeneities in the pore structure on gas flow and dispersion with ^{129}Xe as the gas-phase sensor. The observed chemical shift allows the separate visualization of unrestricted xenon and xenon confined in the pores of the aerogel. The asymmetrical nature of the dispersion pattern alludes to the existence of a stationary and a flow regime in the aerogel. An exchange time constant is determined to characterize the gas transfer between them. As a general methodology, this technique provides insights into the dynamics of flow in porous media where several phases or chemical species may be present.

Understanding multiphase fluid transport in porous materials is necessary to gain insight into a wide range of physical processes, from drug delivery and distribution in blood vessels[1], fluid mixing in chemical reactors[2], to fuel and exhaust transport in fuel cells[3]. General methods for mapping the dynamics of multicomponent flow are rare, primarily owing to the difficulty of probing past the surface layer and in distinguishing between different chemical species[4]. Studies of flow in porous materials, therefore, are often misleading because they generally only provide bulk structural information, such as pore volumes and pore sizes, or kinetic and thermodynamic properties, whereas it is the microscopic structure that determines transport properties[5].

Silica aerogel is a low-density material with a high porosity and a large internal surface area that has been studied extensively owing to its unique structural, elastic, optical and thermal properties[6,7]. Many applications for aerogels have been proposed ranging from biocompatible scaffolds as biosensors[8], aerosol[9] and chemical[10] detectors, to catalytic substrates[11] and gas-adsorption media[12]. Its preparation involves sol–gel hydrolysis followed by condensation, solvent exchange and supercritical drying[13]. Densities typically range from 0.003 to 0.25 g cm^{-3}, whereas specific surface areas can be[14] as large as 1,000 m^2 g^{-1}. Aerogel is built of small, microporous (<2 nm) particles that aggregate to form a large, fractal network[15,16]. This network is mesoporous (2–50 nm) and builds clusters, which themselves aggregate[17] to constitute macropores (>50 nm).

Different techniques are used to characterize the pore structure of aerogels. Neutron- and X-ray-scattering methods[15,16] provide information about various structural features such as mean particle and pore sizes and their distribution, network morphology or the determination of the skeletal density. However, the pore connectivity, which is important for fluid flow, is not directly accessible. Transmission electron microscopy (TEM)[18] and atomic force microscopy (AFM)[17] provide a detailed picture of the pore space on the surface, but only examine a very limited region of the sample. Adsorption, permeability and dynamic gas-expansion experiments[19] are common methods to obtain
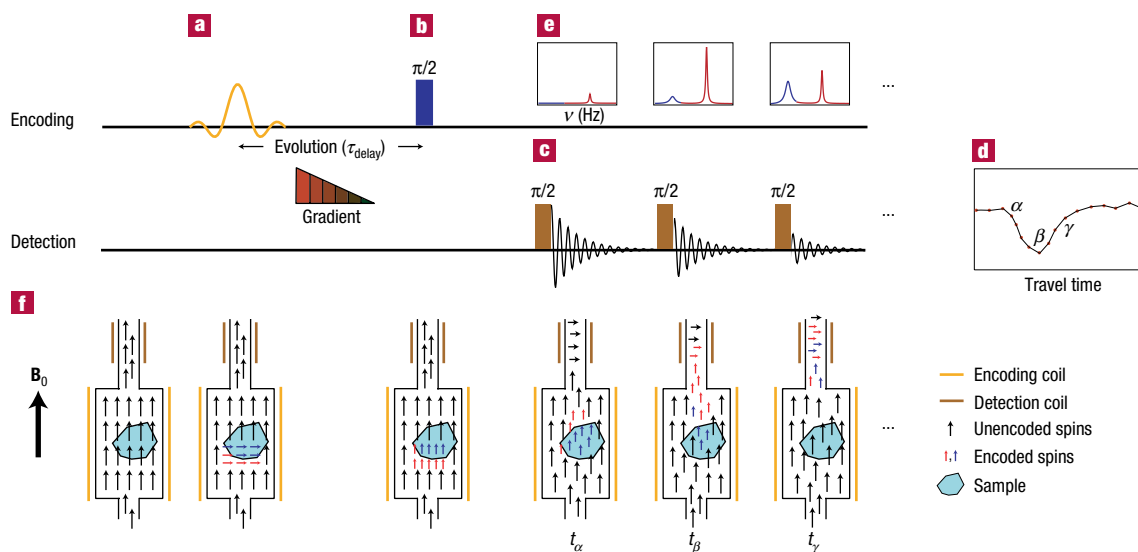
Figure 1 Schematic of a basic remote-detection pulse sequence. The spins initially point along the static magnetic field, B_0, parallel to the flow direction. **a**, A radiofrequency pulse excites the spins of interest, corresponding to a selective tagging of the fluid. Depending on the intensity, the duration and the shape of the pulse, all spins or only spins in a certain spectral region are affected. **b**, After an evolution period, τ_{delay}, a $\pi/2$ pulse is applied, effectively storing one component of the magnetization along B_0 and thereby preventing its dephasing as the spins flow through field gradients to the detector. **c**, As the spins travel to the detection region, a train of $\pi/2$ detection pulses is applied at regular intervals to measure the time at which encoded spins arrive at the detection coil. **d**, The amplitude of each free induction decay provides one point of the TOF curve indicating the fraction of encoded spins in the detection volume at a certain time. The TOF pattern provides information about fluid flow, velocity and dispersion. **e**, Indirect dimensions are recorded point-by-point by varying specific parameters in subsequent encoding steps: τ_{delay} is increased to obtain a spectrum, whereas spatial selectivity can be obtained by applying field gradients during a fixed τ_{delay}. A separate spectrum or image is recorded for each recorded TOF, allowing the spatial dimensions to be correlated with the TOF dimension. **f**, Illustration of the fluid displacement during a TOF experiment. Spins inside the sample (blue) experience a different chemical shift and, therefore, acquire a different phase during τ_{delay} than spins outside the sample (red). The variation of the spin magnetization by the encoding step causes a changing signal as encoded spins flow through the detection coil.

average pore dimensions and pore connectivity. These techniques provide reliable relative pore dimensions when comparing different samples, but the results systematically vary from scattering data. Despite extensive research over the past two decades in this field, determining how the microscopic structure relates to aerogel's unique chemical and physical properties has proved a tremendous challenge[20]. One reason seems to be the difficulties in distinguishing between mesopores and macropores with the established analytical methods.

Most spectroscopic methods are of limited use for the study of aerogels as they require optical access past the surface layer. NMR and magnetic resonance imaging (MRI), on the other hand, are especially suited to study opaque or otherwise optically inaccessible materials[21,22], as long as radiofrequency radiation can penetrate the material and provided that spin-active nuclei are present. The high porosity of aerogel allows the use of a tracer compound, such as ^{129}Xe gas, to act as a sensor of its structure and chemistry[23,24]. Several studies have attempted to link the chemical shift shown by ^{129}Xe in contact with aerogel with its structural characteristics[5,25]. In some cases, several peaks were observed with widely varying linewidths[26], depending on the exact nature of the sample. Although for micropores the chemical shift is expected to reflect the void space available to the xenon atom[27], the smaller chemical shift values observed in mesopores and macropores depend on the pore geometry, the sorption energy and the temperature[25,28]. However, as a general rule, for a given material a larger chemical shift always corresponds to a smaller pore size[29].

The sensitivity of NMR experiments of porous samples can be improved by physically separating the encoding and detection steps, which allows the individual optimization of each[30]. With

this remote detection, information about a stationary sample is encoded onto the spin magnetization of a flowing NMR-active sensor medium[31,32], which is read out with an optimized detector as the sensor medium flows out of the sample. The sensitivity ratio between remote and direct detection is proportional to the relative signal-to-noise ratio as obtained with each probe using an identical sample in a reference experiment[33].

Remote detection is particularly useful for fluid-flow studies[34], where spectroscopic or imaging information about a porous environment can be correlated with the time-of-flight (TOF) of the fluid from its encoding location to the detector[35,36]. This gives a spatially or spectrally resolved dispersion pattern, effectively mapping the flow field. For each encoding step, the TOF can be resolved stroboscopically by applying several detection cycles as the fluid flows through the detector (Fig. 1).

In this work, we apply remote-detection MRI with chemical-shift-selective encoding to distinguish between xenon gas occluded in the aerogel's silicate matrix and free gas that flows without impediment. Differences in the dispersion patterns of xenon inside and outside the aerogel are used to model the flow, and the local gas-flow velocity allows for estimation of the effective porosity of the aerogel. When taking into account known structural properties of the aerogel, the flow features can be correlated with the structure of the material. Our technique makes this possible despite the fact that the spatial resolution of the image encoding is several orders of magnitude too low to resolve the aerogel's pore structure.

Figure 2a shows a ^{129}Xe NMR spectrum recorded remotely with continuously flowing gas and a two-dimensional (2D) representation of the spectral versus the TOF dimension. A distinct aerogel peak is apparent approximately 40 p.p.m. downfield from
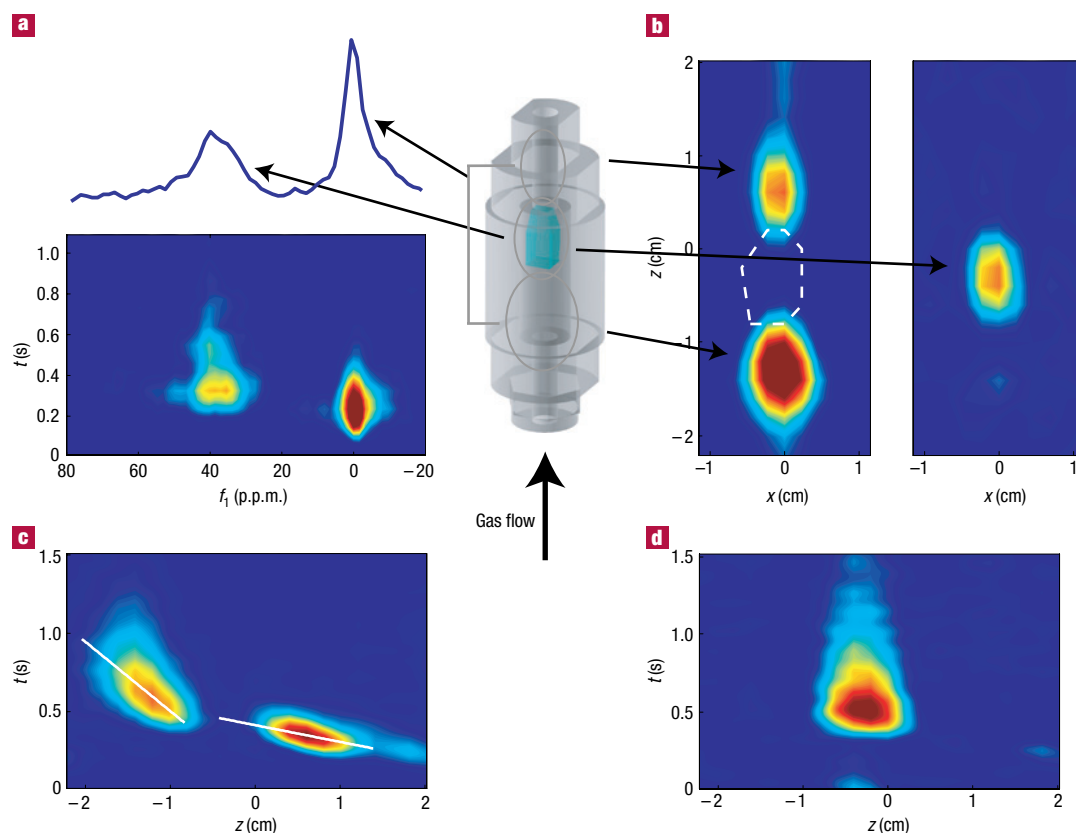
Figure 2 Chemical shift as contrast property to distinguish spins inside and outside the aerogel. a, One-dimensional ^{129}Xe NMR spectrum and the corresponding TOF-resolved spectrum of xenon flowing through aerogel. In this experiment, a non-selective $\pi/2$ pulse encoded all of the spins. The resultant interferogram was obtained in the indirect dimension by arraying the delay time between encoding and storage to obtain information about all chemical-shift species. As shown in the schematic on the right, the aerogel, whose outline is plotted in turquoise, was held in place by a Teflon sample holder. **b,** Chemical-shift-selective image projections corresponding to the free-gas signal (left) and the aerogel signal (right), averaged along the TOF dimension and along y from the full, 4D data sets. **c,d,** TOF of spins encoded in slices perpendicular to the flow direction, z. Chemical-shift selective pulses were applied to either free xenon (**c**) or occluded xenon (**d**). White lines through the inlet and outlet region of the sample container indicate the least-squares regression line or the mean flow velocity in each region along z. Highest intensity for false-colour images is shown in red.

the free-gas peak, corresponding to a mesoporous average pore size in the range of[29] 20–30 nm. A schematic of the aerogel sample and sample housing is shown in the centre of the figure. The flow direction is parallel to the static magnetic field pointed along z.

The chemical-shift-selective image projections corresponding to the two signals onto a plane perpendicular to the lateral y dimension are shown in Fig. 2b. By applying a selective radiofrequency pulse at the appropriate frequency, only spins from a select region of the spectrum were excited. The 2D data sets in Fig. 2c,d show the TOF of the free-gas and the aerogel signal, spatially resolved along the flow dimension. The width of the shapes in the TOF dimension indicates the extent of dispersion, whereas the slope is a measure of the flow velocity. The longitudinal flow velocity of the free gas at the inlet, $v_i = 2.5 \pm 0.6$ cm s^{-1}, is about a factor of four slower than that at the outlet, $v_o = 10.4 \pm 0.6$ cm s^{-1}, as the diameter of the tube at the inlet is a factor of two wider than at the outlet. The shapes are consistent with unrestricted flow[37], with the gas from the inlet showing more dispersion than the gas from the outlet as the former has a longer flow path; it must flow through the aerogel and pass the tube-narrowing constriction at the outlet. The downfield signal shows a qualitatively different behaviour: it remains inside the sample for a time longer than it takes most of the free gas from the inlet to reach the detection region.

Full 3D isosurfaces of the data are shown in Fig. 3. The displacement of the free gas (red) is as expected for convective flow, with the TOF proportional to the distance from the detector. The gas experiencing the downfield chemical shift (blue) lingers inside the aerogel, moving forward much more slowly than expected from the mass flow rate of the gas. Note that whereas isosurface plots provide a good visual impression of transient processes, they are less suited for more quantitative analyses in experiments that involve dispersion because as the signal broadens its amplitude decreases, along with the volume surrounded by the isosurface.

Figure 4 shows snapshots of free gas using a slice-selective phase encoding pulse sequence[35] with an increased spatial and temporal resolution. In the first image, only spins located at the outlet side of the sample are visible. For longer TOF, gas from the inlet side gradually reaches the detector. No significant signal intensity from the free gas is observed inside the centre of the aerogel. However, this signal does not simply disappear as free gas reaches the aerogel and reappear at a time predicted by the sample volume and gas flow rate. Rather, it reappears almost immediately on the other side of the sample, much faster than expected. A rough estimate revealed the average flow velocity of gas in the aerogel to be a factor of seven faster than expected with unrestricted flow in void space of the same volume. The rapid flow velocity indicates a channelling
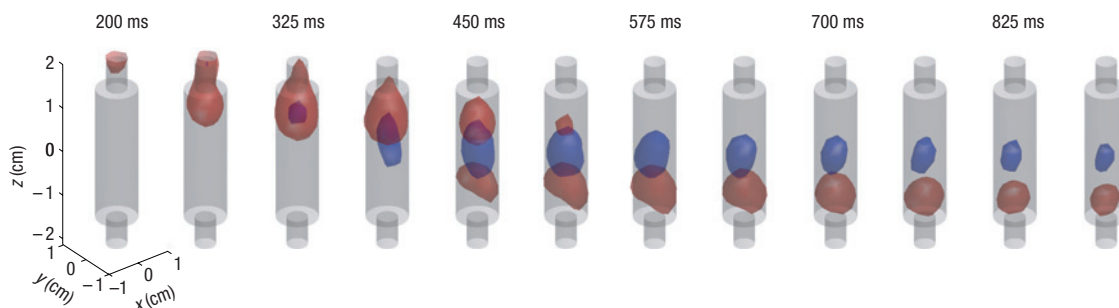
Figure 3 Time-resolved multiphase flow visualization. 3D isosurfaces of occluded (blue) and free gas (red) up to 1 s between encoding and detection. Each image corresponds to the location of the gas during the encoding sequence, ordered with increasing TOF as indicated above the images.

mechanism in a well-connected pore network without significant flow resistance for the main fraction of the gas flowing through the aerogel sample. This strongly contradicts the observed lingering of the downfield signal, which indicates that some of the xenon remains occluded inside the aerogel for a long time, presumably in a different pore regime.

To model the hydrodynamic dispersion of the two signals, which describes the spreading of a fluid due to the combined effects of convective flow and random diffusion, it is helpful to examine the TOF curves from selected locations in the encoding region. Figure 5a shows TOF dispersion curves of free gas from voxels at the inlet and the outlet of the aerogel, and Fig. 5b shows the same data of occluded gas from a voxel inside the aerogel. Without flow resistance, dispersion is mainly due to laminar flow inside the cylindrically shaped tubing on either side of the aerogel sample.

Dispersion is commonly described as a measure of the fluid spreading during a given time interval[37]. An equivalent description can be made by examining the arrival time distribution of a flowing fluid, tagged at one location and observed at a fixed downstream location. The 4D data sets available in our experiments, in principle, contain dispersion information in the spatial as well as temporal domain without any conversion. Dispersion in the spatial domain in an unrestricted geometry can be modelled by a normal distribution[37], centred about its mean value. In the time domain, an analytical description reveals that a normal distribution is only an approximate model, which becomes less valid at very slow flow velocities or very short flow distances. As shown in Fig. 5a, it is found experimentally that the dispersion curve at the outlet can be well-modelled with a normal distribution, $s(t, \mathbf{r}) \approx s_0(\mathbf{r})\Delta t \exp(-(t - t_0(\mathbf{r}))^2 / 2\sigma(\mathbf{r})^2)/\sqrt{2\pi}\sigma(\mathbf{r})$, where $s_0(\mathbf{r})$ is the signal amplitude proportional to the spin density of the encoded spins at the spatial coordinate $\mathbf{r}$ of the encoded spins, t is the TOF between encoding and detection, Δt is the time between detection pulses, which defines the temporal resolution of the TOF dimension, $\sigma(\mathbf{r})^2$ is the variance of the signal distribution in the time domain and t_0 is the centre of the dispersion pattern. This approximation is valid if $\Delta t \leq \sigma(\mathbf{r})$. Both t_0 and σ depend on $\mathbf{r}$ as they are functions of the flow path. Owing to the constrictions in the flow path, it is not straightforward to interpret σ or correlate it with the molecular diffusion coefficient D_0. However, t_0 and the knowledge of $\mathbf{r}$ in our experiments can be used to calculate the mean longitudinal flow velocity as $v(z) = \Delta z/\Delta t_0$, where $\Delta z = z_n - z_{n-1}$ is the distance between adjacent data points, n and $n - 1$, along the z dimension, and $\Delta t_0 = t_0(z_n) - t_0(z_{n-1})$ is the mean flow time from points n to $n - 1$ as determined experimentally by the difference between the flow times from the two points to the detector.

The dispersion of the free gas at the inlet can also be modelled reasonably well with a normal distribution. The dispersion of the gas originating within the aerogel, however, deviates greatly from a normal distribution, and its width is broader than the width of the free gas from the inlet of the aerogel whose flow path is necessarily longer. As in a homogeneous medium the dispersion must increase with time and distance travelled, a decreasing dispersion width with increasing flow distance indicates the existence of two different flow paths with different dispersion mechanisms, path lengths or flow velocities. Examination of the rising edge of the dispersion pattern in Fig. 5b reveals that it has a slope comparable to the free gas, but its tail is significantly longer. An explanation could be the existence of two loosely connected pore regimes, one consisting of fully interconnected pores forming the main flow field and the other consisting of either dead-end pores or pores with a significantly higher flow resistance. To leave this second pore regime, xenon atoms first need to diffuse into the interconnected pore regime, where they have a low probability of being occluded again, and exit the sample with the same velocity as the xenon that never gets occluded. Such a two-step outflow would explain the asymmetric TOF dispersion of the peak at 40 p.p.m.

To model the dispersion pattern of the occluded gas, let us assume that the total exchange of xenon between the two domains is constant in time and that the amount of encoded gas being released into the flow field is proportional to the number of encoded xenon atoms still being occluded a time T after the encoding step. The encoding step itself can be considered to happen instantaneously and the probability function for the xenon release becomes $P(T, \mathbf{r}) = \exp[-T/\tau(\mathbf{r})]/\tau(\mathbf{r})$, with the exchange time constant $\tau(\mathbf{r})$. The observed signal can be calculated by convoluting $P(T, \mathbf{r})$ and $s_0(t - T, \mathbf{r})$ of the free gas from the same location as

$$
\begin{aligned}
\tilde{s}(t, \mathbf{r}) &= \frac{s_0(\mathbf{r})}{\sqrt{2\pi}\tau(\mathbf{r})\sigma(\mathbf{r})} \int_0^\infty \exp\left(-\frac{T}{\tau(\mathbf{r})}\right) \\
&\quad \times \exp\left(-\frac{(t - t_0(\mathbf{r}) - T)^2}{2\sigma(\mathbf{r})^2}\right) \mathrm{d}T \\
&= \frac{s_0(\mathbf{r})}{2\tau(\mathbf{r})} \exp\left(\frac{\sigma(\mathbf{r})^2}{2\tau(\mathbf{r})^2} - \frac{t - t_0(\mathbf{r})}{\tau(\mathbf{r})}\right) \\
&\quad \times \left[1 - \mathrm{erf}\left(\frac{\sigma(\mathbf{r})}{\sqrt{2}\tau(\mathbf{r})} - \frac{t - t_0(\mathbf{r})}{\sqrt{2}\sigma(\mathbf{r})}\right)\right]. \quad (1)
\end{aligned}
$$

This model is illustrated in Fig. 5c. Using this expression, the dispersion curves of occluded gas can be modelled reasonably well (Fig. 5b). Note that whereas the occluded gas is directly observable,
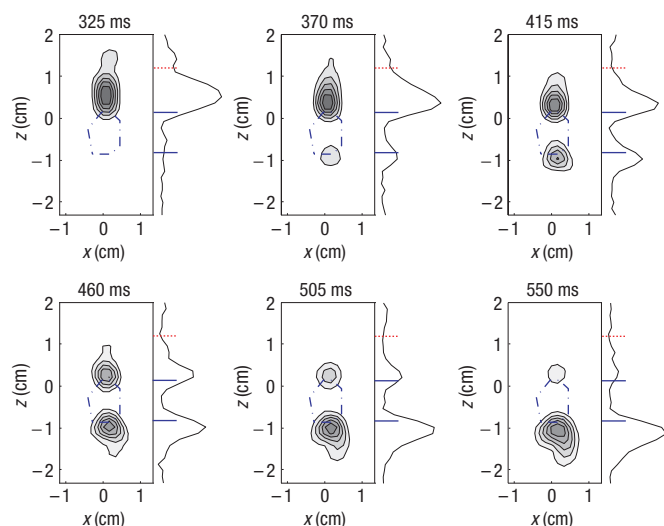
Figure 4 Slice-selective TOF images of free gas. 2D images of free gas in a 0.5 cm slice parallel to the sample axis at different TOF. The outline in blue indicates the location of the aerogel sample as determined from selectively exciting only occluded spins. The projection of the signal onto the z axis is shown alongside each image. The red line indicates the position of a constriction in the outlet flow path. A further chemical-shift-selective pulse was not necessary because the chemical shift difference between the two signals caused the slice of the aerogel signal to be outside the sample.

Figure 5 Dependence of hydrodynamic dispersion on the origin of xenon during encoding. a, Dispersion of free xenon encoded at the outlet ($\times$) and inlet ($\triangle$) of the aerogel. The parameters obtained from fits of a normal distribution to each of the two data sets (black curves) were $t_0 = 0.41 \pm 0.02$ s and $\sigma = 0.08 \pm 0.01$ s for the outlet data, and $t_0 = 0.53 \pm 0.02$ s and $\sigma = 0.12 \pm 0.03$ s for the inlet data. The data were fitted with a nonlinear least-squares minimization using the Levenberg–Marquardt method[40]. **b**, Dispersion of occluded gas in the centre of the sample ($\circ$). Signal intensity is present even after the last detection pulse is applied. A fit using equation (1) provided $t_0 = 0.413 \pm 0.003$ s, $\sigma = 0.07 \pm 0.02$ s and $\tau = 0.62 \pm 0.04$ s (magenta line). **c**, Modelling of the dispersion of the aerogel signal as a convolution ($\otimes$) of a contribution with a gaussian distribution, corresponding to gas that passes without impediment (left), and a stationary, occluded component that is depleted with a time constant τ (middle). Once released into the flow field, the gas flows out of the aerogel undergoing the same dispersion as gas that flows through the aerogel without ever getting occluded. The resulting TOF pattern (right) is scaled to the same total area as the gaussian profile on the left, as expected for an equal local xenon concentration.

the existence of a separate flow-field domain can only be probed indirectly with the current data: $\tau(\mathbf{r})$ quantifies the connectivity between two different pore domains within the sample, whereas $t_0(\mathbf{r})$ and $\sigma(\mathbf{r})$ characterize the nature of the main flow field. The knowledge of the spatial dependence of t_0 enables an estimate of the local longitudinal flow velocity v_a inside the aerogel and also how well a certain volume element in the aerogel is connected to the flow field. By comparing this velocity with the xenon velocity at the outlet of the sample, the effective porosity ϕ_e, that is, the volume fraction of the pore space that is fully interconnected and contributes to the fluid flow through the aerogel, can be calculated as $\phi_e = r v_o / v_a$, where $r \approx 0.25$ is the ratio of the cross-sectional areas of the outlet tube and the aerogel. Experimentally, $v_a = 23.5 \pm 3$ cm s^{-1} was obtained as an average value for the whole sample, giving $\phi_e \approx 0.11 \pm 0.02$. Comparing $\sigma(\mathbf{r})$ of occluded and free gas at locations at the aerogel surface where both are visible reveals similar values for the two. This further supports the model that occluded gas diffuses out of loosely connected pores into the flow field.

We can use equation (1) to fit the TOF curve of each voxel inside the aerogel individually. Figure 6a shows τ in different slices perpendicular to the gas-flow direction. A uniform value of τ is not obtained throughout the sample volume. As a general trend, τ along z is largest in the centre, where it shows a large distribution of different values in the plane perpendicular to z, whereas it decreases towards the inlet and outlet, where it shows much more uniform values. Inside the sample, large heterogeneities can be observed that are seemingly uncorrelated with the distance from the sample wall. It is likely that heterogeneities in the pore connectivity of the sample are responsible for these latter effects. Structural defects such as cracks or fissures are less likely as these would manifest themselves as further signal in the free-gas images and at the same time regions of depleted signal in the occluded-gas images, which is not observed.
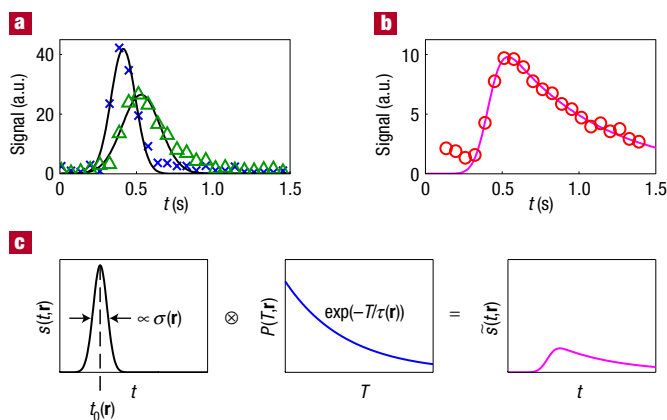
Fitting t_0 over the whole sample reveals major heterogeneities as well, as shown in Fig. 6b. The variation of t_0 within a single slice can be remarkably large, indicating local variations of the flow velocity. This could be caused by a varying permeability of the pore network that constitutes the flow field, suggesting the existence of pores with a large spatial variation of diameters. However, as the flow field could be characterized only indirectly, further investigation is warranted.

From the estimated value of ϕ_e, one would expect a significant signal from xenon in the flow field. As the signal of the free gas vanishes almost completely inside the aerogel, it seems possible that ^{129}Xe in pores constituting the flow field covers a similar spectral region as xenon that is stationary in the aerogel, but perhaps experiences a broader linewidth. This would be consistent with a structural model that distinguishes between mesopores and macropores. In light of these data, it may be useful to distinguish these two pore domains not purely by their diameter, but also by their connectivity.

As $\sigma(\mathbf{r})$ and $t_0(\mathbf{r})$ both characterize the main flow field, one expects them to be correlated to some degree, whereas the presence of correlation between $t_0(\mathbf{r})$ and $\tau(\mathbf{r})$ would indicate structural interrelations between the pore domains. As can be seen by comparing Fig. 6a and b, there is no obvious correlation between t_0 and τ, which indicates that heterogeneities of the pore domains are not necessarily related. In Fig. 6d, this lack of correlation is visualized by plotting τ versus t_0 of the different data points. In contrast, plotting σ versus t_0 (Fig. 6c) shows a clear correlation between the two. However, this correlation is relatively noisy, which could be explained if structural heterogeneities responsible for the
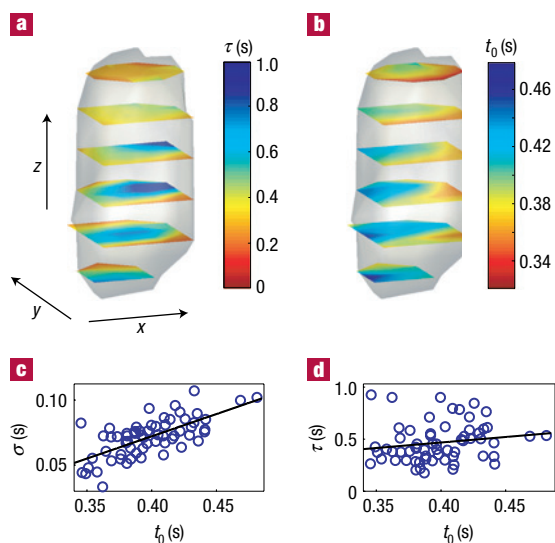
Figure 6 Heterogeneity of hydrodynamic dispersion: probing pore space variations of the aerogel. a, τ in different slices through the aerogel perpendicular to z. Red colours correspond to short τ and blue to long τ, as shown by the colourbar. The grey shade outlines the aerogel sample. **b**, Analogous representation of t_0 in different slices perpendicular to z. **c**, Plot of σ versus t_0. A linear regression gives a correlation coefficient of 0.7. **d**, Plot of τ versus t_0. No significant correlation could be identified between the two parameters.

variation of t_0 and σ were on a smaller length scale than the resolution of the image, as a distribution of different t_0 tends to broaden σ. Data in ref. 23 indicate that this is a realistic option.

TOF NMR studies with remote detection, using the chemical shift as a contrast property, was shown to be a powerful tool for studying fluid flow inside nanoporous materials. Chemical selectivity was achieved either by using selective pulses to address only nuclei with a certain resonance frequency, or by resolving the full spectrum of the sample as a further experimental dimension. This method may prove valuable to analyse fluid flow and retention in a large range of other porous materials, notably zeolites, clathrates or porous glasses, as a chemical shift of ^{129}Xe can be generally observed[27–29] in nanoporous environments with pore sizes below about 50 nm.

The TOF dispersion of xenon gas encoded inside the aerogel was introduced as a further contrast property to study the void-space structure of porous media. It allowed two different pore domains to be distinguished, one accommodating the convective flow field and the other containing xenon that is diffusively exchanging with this flow field. Most of the gas passes through the sample, without ever leaving the flow field, at an elevated velocity owing to a reduced effective porosity of these pores, whereas the larger fraction of gas that is inside the sample at any time is in the diffusive regime with a much longer residence time. This could be explained by the existence of closed pores that are poorly interconnected to a network of open pores. This would also explain the discrepancy between gas-expansion experiments, which commonly use a capillary model to interpret the data, and scattering experiments in predicting average pore dimensions[19]. It seems plausible to identify the closed pores as mesopores and the open pores as macropores, but we do not have direct evidence for this assignment yet.

The transient detection of dispersion in combination with imaging allows local time constants to be measured, which can be used to obtain spatially resolved values of what are typically considered bulk-material properties and thereby identify material heterogeneities. The similarity of this technique to chromatography may help in developing more-refined theoretical models to explain the observed dispersion patterns, whereas the spatial selectivity offered by MRI encoding may prove useful as an experimental tool to identify heterogeneities in the pore connectivity of stationary phases.

This methodology is not restricted to the chemical shift of ^{129}Xe in contact with a particular chemical species or surface, but is applicable to nearly any fluid with spin-active nuclei. This includes liquids, with ^{1}H as the most apparent target nucleus because of its abundance in many fluids and organic molecules. ^{1}H covers a much smaller chemical shift range than ^{129}Xe and is therefore not selective enough to distinguish between different pore environments. However, ^{1}H in different molecular environments typically experience resolvable chemical-shift differences, which allow NMR to distinguish between multiple components of fluid mixtures. As these chemical shifts do not depend on the porous material to be studied, the chemical-shift selection can be done in the encoding as well as in the detection environment. This enables chemical-shift selectivity even in encoding environments where the chemical shift is not resolvable, for instance, at low magnetic fields or in cases of significant susceptibility gradients common in porous rocks, as long as detection is done in a high-field, high-resolution environment. Motivations for low-field encoding could be portability and cost, or the presence of an electrical conductor in the sample with a reduced skin depth for radiofrequency penetration. Applications of this method include the study of fluid transport, mixing or reaction monitoring in porous environments as diverse as minerals, microfluidic devices or catalytic converters. This illustrates that combining chemical-shift-selective MRI with TOF remote detection is both uniquely applicable to study nanoporous materials, and adaptable as a versatile and general methodology for studying fluid dynamics inside materials with arbitrary pore size.

METHODS

CHEMICALS

The silica aerogel sample had a density of $0.008-0.009$ g cm^{-3} and measured roughly 0.5 cm^3 in volume. The gas mixture contained 1% Xe (natural abundance), 10% N$_2$ and 89% He.

EXPERIMENTAL SETUP

All experiments were performed on a Unity Inova NMR spectrometer (Varian, Palo Alto, California) at a magnetic field of 7.05 T, corresponding to a ^{129}Xe frequency of 82.9 MHz. The home-built detection probe with a 10 mm diameter saddle coil was placed on top of the magnet, whereas the microimaging probe (Varian, Palo Alto, California), using a 40 mm birdcage coil, was placed inside an actively shielded gradient stack (Resonance Research, Billerica, Massachusetts) from below. The detection coil was about a factor of three more sensitive than the encoding coil. The upper rim of the encoding and the lower rim of the detection coils were separated by approximately 2 cm. The detection coil was kept inside an isolating copper shield to minimize mutual couplings with the encoding coil. The sample was housed in a Teflon casing and was surrounded by clay to keep it stationary and to prevent flow around the sample. The sample housing had an outlet diameter of 6.3 mm and an inlet diameter of 12.7 mm. A XenoSpin polarizer (Amersham Health, Durham, North Carolina) was used to optically pump ^{129}Xe to about 10% spin polarization, corresponding to an increase of about four orders of magnitude compared with its equilibrium value at 7 T. The gas mixture then flowed through the sample, where ^{129}Xe was encoded. After passing the detection coil it was vented to the atmosphere. The pressure and flow rate could be controlled using valves on the inlet and outlet sides of the sample[38]. The imaging data were obtained at a pressure of 4.0 bar and 0.65 standard litre per minute mass

flow rate, whereas the spectroscopic TOF data were obtained at a pressure of 2.0 bar at the same mass flow rate.

PULSE SEQUENCES

2D spectroscopic data were obtained by applying a non-selective $\pi/2$ excitation pulse followed by a variable time delay before the application of another $\pi/2$ pulse to prevent the spin magnetization from dephasing as it flows to the detector. As the ^{129}Xe arrived at the detection region, its time-resolved magnetization was measured using a train of $\pi/2$ pulses separated by 50 ms. 3D imaging data and their respective projection were obtained by phase encoding along x, y and z with a field of view (FOV) of 2.75 cm × 2.75 cm × 4.5 cm and a resolution of 4.6 mm along x, y and 4.0 mm along z, using field gradient pulses of 100 µs length in all three spatial dimensions between a selective encoding pulse and a non-selective storage pulse at the end of the encoding sequence. The time resolution in the TOF dimension was 62.5 ms. For chemical-shift selectivity, a gaussian-shaped excitation pulse with a bandwidth of 2 kHz, corresponding to 24 p.p.m., was used. Slice-selective phase encoding data in Fig. 4 were obtained by phase encoding along x and z with a FOV of 3 cm × 5 cm and a resolution of 3.3 mm, while selecting a 0.5 cm slice of spins along y with a sinc-shaped encoding pulse in the presence of a y-gradient. The time resolution was 45 ms. In all experiments, a four-step phase cycle was used to obtain frequency discrimination in the indirect dimensions and to remove the baseline caused by unencoded gas[39]. A full 4D experiment took less than one hour, whereas a 2D spectroscopic experiment could be performed in about eight minutes.

References

1. Jang, S. H., Wientjes, M. G., Lu, D. & Au, J. L.-S. Drug delivery and transport to solid tumors. *Pharm. Res.* **20,** 1337–1350 (2003).
2. Gladden, L. F., Lim, M. H. M., Mantle, M. D., Sederman, A. J. & Stitt, E. H. MRI visualization of two-phase flow in structured supports and trickle-bed reactors. *Catal. Today* **79,** 203–210 (2003).
3. Steele, B. C. H. & Heinzel, A. Materials for fuel-cell technologies. *Nature* **414,** 345–352 (2001).
4. Mair, R. W., Tseng, C.-H., Wong, G. P., Cory, D. G. & Walsworth, R. L. Magnetic resonance imaging of convection in laser-polarized xenon. *Phys. Rev. E* **61,** 2741–2748 (2000).
5. Gregory, D. M., Gerald, R. E. & Botto, R. E. Pore-structure determinations of silica aerogels by ^{129}Xe NMR spectroscopy and imaging. *J. Magn. Reson.* **131,** 327–335 (1998).
6. Gibiat, V., Lefeuvre, O., Woignier, T., Pelous, J. & Phalippou, J. Acoustic properties and potential applications of silica aerogels. *J. Non-Cryst. Solids* **186,** 244–255 (1995).
7. Hua, D. W., Anderson, J., Di Gregorio, J., Smith, D. M. & Beaucage, G. Structural analysis of silica aerogels. *J. Non-Cryst. Solids* **186,** 142–148 (1995).
8. Power, M., Hosticka, B., Black, E., Daitch, C. & Norris, P. Aerogels as biosensors: viral particle detection by bacteria immovilized on large pore aerogel. *J. Non-Cryst. Solids* **285,** 303–308 (2001).
9. Guise, M., Hosticka, B., Earp, B. & Norris, P. M. An experimental investigation of aerosol collection utilizing packed beds of silica aerogel microspheres. *J. Non-Cryst. Solids* **285,** 317–322 (2001).
10. Sumiyoshi, T. *et al.* Silica aerogels in high energy physics. *J. Non-Cryst. Solids* **225,** 369–374 (1998).
11. Fricke, J. (ed.) in *Aerogels* (Springer Proceedings in Physics, Vol. 6, Springer, Berlin, 1986).
12. Hosticka, B., Norris, P. M., Brenizer, J. S. & Daitch, C. E. Gas flow through aerogels. *J. Non-Cryst. Solids* **225,** 293–297 (1998).
13. Hunt, A. J. & Lofttus, K. D. in *Better Ceramics Through Chemistry III* (eds Brinker, C. J., Clark, D. E. & Ulrich, D. R.) 679–684 (Materials Research Society Symposia Proceedings, Vol. 121, Materials Research Society, Pittsburgh, 1988).
14. El Rassy, H. & Pierre, A. C. NMR and IR spectroscopy of silica aerogels with different hydrophobic characteristics. *J. Non-Cryst. Solids* **351,** 1603–1610 (2005).
15. Emmerling, A. & Fricke, J. Small angle scattering and the structure of aerogels. *J. Non-Cryst. Solids* **145,** 113–120 (1992).
16. Schaefer, D. W. & Keefer, K. D. Structure of random porous materials: silica aerogel. *Phys. Rev. Lett.* **56,** 2199–2202 (1986).
17. Marlière, C. *et al.* Very large-scale structures in sintered silica aerogels as evidenced by atomic force microscopy and ultra-small angle X-ray scattering experiments. *J. Non-Cryst. Solids* **285,** 148–153 (2001).
18. Ruben, G. C., Hrubesh, L. W. & Tillotson, T. M. High-resolution transmission electron microscopy nanostructure of condensed silica-aerogel. *J. Non-Cryst. Solids* **186,** 209–218 (1995).
19. Reichenauer, G., Stumpf, C. & Fricke, J. Characterization of SiO_2, RF and carbon aerogels by dynamic gas expansion. *J. Non-Cryst. Solids* **186,** 334–341 (1995).
20. Gavalda, S., Kaneko, K., Thomson, K. T. & Gubbins, K. E. Molecular modeling of carbon aerogels. *Colloids Surf. A* **187,** 531–538 (2001).
21. Callaghan, P. T. *Principles of Nuclear Magnetic Resonance Microscopy* (Oxford Univ. Press, Oxford, 1993).
22. Mair, R. W. *et al.* Probing porous media with gas diffusion NMR. *Phys. Rev. Lett.* **83,** 3324–3327 (1999).
23. Kaiser, L. G., Meersmann, T., Logan, J. W. & Pines, A. Visualization of gas flow and diffusion in porous media. *Proc. Natl Acad. Sci. USA* **97,** 2414–2418 (2000).
24. Guillot, G., Nacher, P.-J. & Tastevin, G. NMR diffusion of hyperpolarized ^{3}He in aerogel: a systematic pressure study. *Magn. Reson. Imag.* **19,** 391–394 (2001).
25. Terskikh, V. V., Mudrakovskii, I. L. & Mastikhin, V. M. ^{129}Xe nuclear magnetic resonance studies of the porous structure of silica gels. *J. Chem. Soc. Faraday Trans.* **89,** 4239–4243 (1993).
26. Moudrakovski, I. L. *et al.* Nuclear magnetic resonance studies of resorcinol-formaldehyde aerogels. *J. Phys. Chem. B* **109,** 11215–11222 (2005).
27. Demarquay, J. & Fraissard, J. Xe-129 NMR of xenon adsorbed on zeolites—relationship between the chemical-shift and the void space. *Chem. Phys. Lett.* **136,** 314–318 (1987).
28. Ripmeester, J. A. & Ratcliffe, C. I. On the application of ^{129}Xe NMR to the study of microporous solids. *J. Phys. Chem.* **94,** 7652–7656 (1990).
29. Terskikh, V. V. *et al.* A general correlation for the ^{129}Xe NMR chemical shift-pore size relationship in porous silica-based materials. *Langmuir* **18,** 5653–5656 (2002).
30. Zax, D. B., Bielecki, A., Zilm, K. W., Pines, A. & Weitekamp, D. P. Zero field NMR and NQR. *J. Chem. Phys.* **83,** 4877–4905 (1985).
31. Moulé, A. J. *et al.* Amplification of xenon NMR and MRI by remote detection. *Proc. Natl Acad. Sci. USA* **100,** 9122–9127 (2003).
32. Seeley, J. A., Han, S. & Pines, A. Remote detected high-field MRI of porous samples. *J. Magn. Reson.* **167,** 282–290 (2004).
33. Granwehr, J. & Seeley, J. A. Sensitivity quantification of remote detection NMR and MRI. *J. Magn. Reson.* **179,** 229–238 (2006).
34. Koptyug, I. V., Altobelli, S. A., Fukushima, E., Matveev, A. V. & Sagdeev, R. Z. Thermally polarized H-1 NMR microimaging studies of liquid and gas flow in monolithic catalysts. *J. Magn. Reson.* **147,** 36–42 (2000).
35. Granwehr, J. *et al.* Time-of-flight flow imaging using NMR remote detection. *Phys. Rev. Lett.* **95,** 075503 (2005).
36. Hilty, C. *et al.* Microfluidic gas-flow profiling using remote detection NMR. *Proc. Natl Acad. Sci. USA* **102,** 14960–14963 (2005).
37. Taylor, G. Dispersion of soluble matter in solvent flowing slowly through a tube. *Proc. R. Soc. Lond. A* **219,** 186–203 (1953).
38. Han, S. *et al.* Improved NMR based bio-sensing with optimized delivery of polarized ^{129}Xe to solutions. *Anal. Chem.* **77,** 4008–4012 (2005).
39. Granwehr, J., Urban, J. T., Trabesinger, A. H. & Pines, A. NMR detection using laser-polarized xenon as a dipolar sensor. *J. Magn. Reson.* **176,** 125–139 (2005).
40. Press, W. H., Teukolsky, S. A., Vetterling, W. T. & Flannery, B. P. *Numerical Recipes in C* 2nd edn (Cambridge Univ. Press, Cambridge, 1992).

Acknowledgements

Competing financial interests